Novel concept of hydroxyl radical generation in hydrodynamic cavitation on a chip

Rana Golshaei [a,b,1], Salar Heyat Davoudian [a,b,1], Erçil Toyran [b], Ezgi Kestek [a,b],
Amanpreet Kaur [d], Abhinav Priyadarshi [d], Ali Koşar [a,b,c,*], Iakovos Tzanakis [d,e,**],
Morteza Ghorbani [a,b,d,**]

[a] Sabanci University Nanotechnology Research and Application Center, 34956 Tuzla, Istanbul, Turkey
[b] Faculty of Engineering and Natural Science, Sabanci University, 34956 Tuzla, Istanbul, Turkey
[c] Center of Excellence for Functional Surfaces and Interfaces for Nano-Diagnostics (EFSUN), Sabancı University, Orhanli, 34956 Tuzla, Istanbul, Turkey
[d] Faculty of Technology, Design and Environment, Oxford Brookes University, Headington, Oxford, OX3 0BP Wheatley, Oxford OX33 1HX, UK
[e] Department of Materials, University of Oxford, Parks Road, Oxford OX1 3PH, UK

ARTICLE INFO

ABSTRACT

In this study, the hydrodynamic cavitation on a chip reactor (HC on a chip), facilitated by two configurations: a micro-orifice and a long diaphragm, was utilized to produce the reactive species, particularly hydroxyl radicals (•OH). The micro-orifice configuration allowing intense localized pressure gradients promotes intense cavitation events, leading to higher yields of •OH per unit energy input (0.6×10^{-6} g/J in comparison to 3.0×10^{-8} g/J for the long diaphragm configuration in the cavitation inception regime). This is advantageous for applications requiring concentrated •OH production, such as advanced oxidation processes. In contrast, the long diaphragm reactor, despite a larger power input (6.4 W at 2.9 MPa compared to 1.5 W for the micro-orifice configuration), provides a more uniform distribution of radicals along its length, based on the temporal trend of I_3^- formation. This shows a gradual and sustained rate compared to the sharp, early peak in the micro-orifice reactor. The lower reaction in Reactor 2 indicates that radical formation occurs over a wider area rather than being localized. This aligns with the geometry and flow pattern of the diaphragm which allows for a larger zone of cavitation and longer bubble activity. Comparative analysis reveals that microscale reactors demonstrate higher reaction rates and sharper peaks in I_3^- production than macroscale reactors, which show higher chemical activity. The orifice possesses the highest maximum peak in the microreactors, and the long diaphragm releases more uniformly distributed radicals, with microscale systems overall having higher energy efficiency and lower energy costs.

1. Introduction

Cavitation is described as the formation, expansion, and subsequent collapse of gas or vapor bubbles due to localized pressure fluctuations. This physical phenomenon occurs when the pressure in a liquid reduces abruptly and below its vapor saturation pressure. The collapse of cavitation bubbles generates a substantial amount of energy ($1–10^{18}$ kW/m^3) in a brief moment, inducing thermal, mechanical and chemical effects in the surrounding liquid [1]. In an aqueous medium, when

cavitation bubbles reach a sufficient size, the pressure difference between the bubble interior and the surrounding medium exceeds the critical threshold, resulting in violent implosion, thereby giving rise to temperatures in excess of 5000 K (hot gas core of the bubble) and pressures reaching 1000 bar [2]. The mechanical effects, such as shock waves (in the GPa range), shear stresses (0.1–10 MPa), high velocity microjets (over 100 m/s) [3], as well as chemical effects such as formation of highly active hydroxyl radicals (•OH) resulting from localized hot spots, could be utilized in a wide range of applications [4].

Based on their generation mechanisms, cavitation phenomena could be classified into two main types: hydrodynamic cavitation (HC) and acoustic cavitation (AC) [5]. While AC is generated by applying ultrasound waves with a cyclic succession of expansion (rarefaction) and compression phases, HC is a continuous phenomenon that occurs when a steady liquid flow passes through a flow constriction or around an obstacle leading to the formation of localized low-pressure regions. Compared to AC, the process of HC has recently gained significant attention particularly for large-scale industrial applications, owing to its advantages in scalability, cost effectiveness, energy efficiency, and simplicity. It has been recently reported that HC can also be an effective tool for chemical and biological applications, e.g., microbial inactivation [6], removal of organic compounds [7], decomposition of waste-activated sludge [8], food processing [9], pharmaceuticals [10], emulsification [11] and exfoliation [12]. Compared to the well-known mechanical effects of bubble collapse (such as shock waves [13–19]), the chemical effects particularly in HC have been rarely investigated [20]. In this regard, the extreme conditions such as high temperatures and pressures in the interior of the bubble can cause the homolytic dissociation of water molecules and decomposition of dissolved oxygen (O_2) molecules in the cavities and formation of highly reactive species, such as hydroxyl radicals ($^\bullet OH$), oxygen atoms ($^\bullet O$), hydrogen atoms ($^\bullet H$), and hydroperoxyl radicals ($HO_2^\bullet$) [21]. The recombination of $^\bullet OH$ and $HO_2^\bullet$ forms hydrogen peroxide (H_2O_2) outside the hot bubbles. In addition, $^\bullet H$ and $^\bullet OH$ species can react with produced H_2O_2 to generate $^\bullet OH$ and $HO_2^\bullet$ [22]. These species play a crucial role in the chemical processes induced by cavitation, as they can break-down complex organic compounds [23], degrade pollutants [24] and initiate oxidation reactions [25]. Additionally, an increase in the number of free radicals in a flow constriction due to the bubble collapse improves the efficiency of the oxidation process [23]. Thus, all these effects make the cavitation phenomenon a multi-functional and versatile sustainable technology.

Despite the challenges associated with quantifying $^\bullet OH$ due to their extremely short lifetimes (~1 ns) [26], there are numerous attempts to quantify their production using a range of dosimeters, including Electron Spin Resonance (ESR) [27], salicylic acid dosimetry [28], Fricke dosimetry [29], terephthalic acid [30], and potassium iodide dosimetry (KI) [31]. However, the highly reactive nature of $^\bullet OH$ makes it a challenging task to capture their behavior before they react with other molecules or decompose. In the context of HC and $^\bullet OH$ detection, KI dosimetry presents several advantages that make it a superior choice for certain applications. KI dosimetry has been inspired by the Weissler reaction as a simple, cost-effective and widely acceptable technique [32], since it can be performed with minimal technical equipment, making it more accessible for routine testing [33]. KI dosimetry is less prone to the interference from other reactive species compared to methods such as salicylic acid dosimetry, which may be affected by other radical species present in the system. In comparison to Fricke reaction and terephthalate dosimetry, KI dosimetry is more efficient and accurate and less complicated [34]. Moreover, KI dosimetry provides direct and real-time measurement of radical production, which can be more convenient for studying transient species in cavitation processes. According to these factors, KI is a well-established reagent for quantifying reactive species, particularly iodine radicals and tracking $^\bullet OH$ during cavitation, which can serve as indicators of the oxidative conditions generated by cavitation. The tri-iodide ion (I_3^-) is a key species in KI dosimetry, characterized by enhanced stability and a distinctive absorbance peak within the UV–visible spectrum, typically observed at 353 nm [35]. Although various studies have utilized KI dosimetry, there is a significant gap regarding the detailed investigation of the $^\bullet OH$ production in HC. Thus, microscale HC could be a perfect concept, due to controlled environment, to investigate the relationship between the HC mechanisms including flow regimes and $^\bullet OH$ production [32,35]. Other reactive oxygen species (ROS) besides $^\bullet OH$ can react with KI, and their contributions need to be taken into account. In particular, superoxide anions ($O_2^{\bullet -}$) can undergo redox reactions with iodide ions (I^-) to

form iodine (I_2). Singlet oxygen ($^1O_2$) and ozone (O_3) can undoubtedly be generated under specific conditions; however, they are not believed to be predominant species in cavitation systems as compared to $^\bullet OH$ [36]. Here, we were most interested in $^\bullet OH$ since they are typically the most reactive and most abundant ROS in cavitation-mediated chemical processes. They are significantly more reactive than O_3 [37] and $O_2^{\bullet -}$ [38], and play a more central role in chemical and environmental cavitation applications.

Besides the chemical aspects of HC bubble collapse, surface topology and device geometry in microfluidic reactors (microscale HC reactors) are also critical parameters that facilitate bubble formation leading to more intense collapses, the enhanced energy release and increased $^\bullet OH$ production [39]. In terms of the influence of reactor geometry on HC behavior, which influences the key parameters that impact the cavitation inception and resulting flow behavior, various studies were performed. For instance, Simpson and Ranade [40] developed computational fluid dynamics models to simulate cavitating flows through orifices. They made detailed comparisons of their findings with experimental results and demonstrated that important parameters—such as the orifice thickness, inlet geometry, and wall angling—have a profound effect on the cavitation inception, pressure recovery gradients, and collapse conditions. Long et al. [41] performed experiments in a venturi tube, measuring and analyzing cavitation stages to demonstrate that a constant critical pressure ratio and cavitation number govern cavity length development, thus, exhibiting a distinct linear correlation with an apparent transition threshold. Medrano et al. [42] highlighted that microchannel geometry, specifically the shape of diaphragms and micro-venturis, plays a decisive role in the transition to two-phase flow and cavitation behavior under high pressure loss conditions. While the configuration and geometry of the reactor significantly influence cavitation behavior, Kerboua et al. [43] demonstrated that maximizing collapse intensity for effective sonochemical activity requires a balance between energy accumulation and condensation. In this context, Hong et al. [44] conducted a numerical investigation of bubble dynamics in a Venturi reactor and found that wall-generated bubbles exhibit the most energetic oscillations, with maximum collapse pressures occurring during the most intense downstream cavitation events. In addition, Lobasov and Kravtsova's [45] mathematical modeling of cavitating flow behind a cylinder—in a comparison of smooth and textured surfaces—illustrated how surface structure, and the presence of triangular prisms in particular, strongly influences cavitation inception, cavity dynamics, and drag coefficients at low to medium upstream pressures. Additionally, Maleki et al. [46] investigated the chemical effects of microscale HC across various microfluidic reactor configurations. Their findings indicate that the reactor geometry regulates the cavitation performance and radical production—wherein the micro-orifice reactor demonstrates a superior performance relative to other configurations owing to intensified flow dynamics and elevated bubble collapse frequencies.

Cavitation behavior differs significantly between microscale and macroscale reactors mainly due to the interactions and dynamics at different scales. Scaling down from macroscale to microscale HC reactors is anticipated to enhance $^\bullet OH$ production. This improvement arises from the intensified bubble dynamics at the microscale, where the rapid expansion and collapse of cavitation bubbles generate significantly higher localized pressures and temperatures. These extreme conditions facilitate the thermal decomposition of water molecules within the cavitation bubbles, thereby increasing the production of $^\bullet OH$ [47,48]. The compact dimensions of microscale HC reactors also allow for precise control over flow patterns and cavitation zones, offering advantages for applications requiring targeted and efficient radical production [49]. This study investigates the influence of reactor geometry on cavitation intensity and $^\bullet OH$ production in microscale HC reactors, using KI dosimetry to assess the chemical effects of cavitation in two microfluidic configurations: micro-orifice and long diaphragm. The findings reveal how reactor design, cavitating flow patterns, and

upstream pressure impact •OH generation, demonstrating that lower pressure drops in microscale HC reactors can effectively promote localized and rapid radical production.

2. Materials and methods

2.1. KI solution preparation

A concentration of *0.1 M* KI was employed for dosimetry to monitor •OH production during cavitation process. Two equal KI solutions with a *0.1 M* concentration were prepared by mixing deionized (DI) water with KI powder sourced from ISOLAB Chemicals (Germany) at 50 rpm for approximately 4 min. One sample was left untreated for reference (No Cavitation), while the others were transferred to the HC test rig and passed through the HC reactor.

2.2. Design and fabrication of microscale HC reactor

The experiments were performed using two microscale HC reactors, micro-orifice (Reactor 1) and long diaphragm (Reactor 2) reactors with different design parameters summarized in Table 1 and Fig. 1. Both reactors consisted of three regions including an inlet channel, an extension channel, and a nozzle that acted as a flow-restrictive element triggering HC formation [50]. Due to the symmetrical design of both reactors, they could be used in both flow directions. When the flow direction was changed, the same cavitating flow pattern could be obtained at the same upstream pressure. Fabrication of microscale HC reactors involved semiconductor based adopted microfabrication techniques. The fabrication process consisted of several key stages: substrate preparation, photolithography, etching, metal deposition, and bonding. Substrate preparation began with RCA (Radio Corporation of America) cleaning of a silicon (Si) wafer, followed by the deposition of a 500 nm thick silicon dioxide (SiO_2) layer on both sides of the substrate. This step ensured insulation and enhanced adhesion for the subsequent processes. Photolithography was conducted with a Süss ACS200 GEN3 coater and MLA 150 developer. A 2 μm layer of ECI 3007 photoresist was applied and patterned, defining the basic structure of the reactor channels and holes. The SiO_2 layer exposed during this process was dry etched on an SPTS APS tool to a depth of 500 nm to establish correct delineation of micro-structures in the reactor. The remaining ECI 3007 photoresist was removed through the combination of Tepla plasma ashing and wet chemical. The metal deposition process involved a two-step sputtering approach, where a 10 nm titanium (Ti) layer was deposited as an adhesion promoter, followed by the deposition of a 1 μm thick aluminum (Al) layer. All the deposition process was performed using the DP650 sputtering system for obtaining homogeneous and controlled formations of a thin metal layer. To achieve higher resolution features, Electron Beam Lithography (EBL) system was employed. A 500 nm layer of ZEP 520A resist was deposited, followed by patterning and then SiO_2 dry etching and resist stripping. The final structure of the reactor was realized via a two-step deep-etching process, where samples were first coated with AZ 10XT-60 photoresist to a thickness of 8 μm, then photolithography was carried out using the MLA 150 system in a rapid
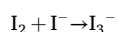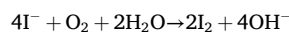
mode for both exposure and development, targeting a controlled deposition of 1800 μm of port layer material. Subsequently, two successive dry etching processes using an SPTS Rapier system were performed with an initial etch to 475 μm depth, followed by a deeper etch down to 60 μm. Al and Ti, as well as remaining SiO_2 layers were removed using Plade Metal and Plade Oxide wet benches. At the final step, anodic bonding was implemented to join the Si substrate with a Borofloat glass wafer, yielding a hermetically sealed reactor. The Borofloat glass wafer, cleaned by Piranha solution (a mixture of concentrated sulfuric acid (H_2SO_4) and H_2O_2, in a ratio of 3:1) to offer ideal bonding conditions. Annealing was then performed using an SB6 machine in order to relieve residual stresses and impart a higher strength to the bond. Fig. 1(a–k) schematically outlines the entire process with step-by-step interconnection of the microscale HC reactor.

2.3. Experimental test rig and experimental procedure

The experimental setup (Fig. 2a) was designed to incorporate the microscale HC reactors (Fig. 2b and c) with a tubing system and proper fittings. The system was fed with different upstream pressures from a high-pressure nitrogen tank, sourced from Linde Gas, Gebze, Kocaeli. The nitrogen tank was connected to a 1-gallon container (Swagelok, Erbusco BS, Italy) filled with a mixture of DI water and *0.1 M* KI solution. In both reactors, the solution temperature was measured by a thermocouple before and after cavitation. Accordingly, it was consistently observed to remain around 22 °C, equivalent to room temperature. This result ensured that temperature variations did not influence •OH production. The fluid reservoir was securely attached to the system using compatible fittings. The pressure within the system was measured using pressure gauges (Omega, USA, range of up to 20.7 MPa) located at the terminal end of the experimental setup as well as on the sandwich assembly holding the reactor. A fine control valve was used to control the flow within the system. Additionally, silicon micro-O-rings were employed at critical junctions to ensure leak-proof action.

Prior to each experimental run, all components, including connectors, valves, device holder, reactor, and associated tubing were thoroughly cleaned to remove any possible contaminants. The samples containing KI were carefully transferred to the sample container shown in Fig. 2 to be exposed to HC inside the microscale HC reactor. As the aim of this study was to investigate the •OH production level under different HC conditions, namely inception, developed and super-cavitation, the upstream pressure (P_{up}) was changed to achieve these flow patterns while the downstream pressure was kept constant at atmospheric pressure. The upstream pressures corresponding to inception, developed and super-cavitation flow condition for Reactor 1 and Reactor 2 were found as 0.52, 1.24, 2.9 MPa and 1.03, 2.07, 2.9 MPa, respectively. For every HC condition, 5 cycles were examined, and each took around 10 min—a timeframe allowed by selecting an appropriate solution volume to prevent time-dependent effects. For each cycle, samples (3 mL) were collected at two time points—minute 4 and minute 8—to effectively capture the evolution of •OH production. Both untreated (No cavitation) and treated samples were analyzed simultaneously using UV–Vis spectroscopy (Varian Cary 5000 UV–Visible-NIR Spectrometer). The experimental conditions for each cavitating flow pattern in both reactors are summarized in Table 2. It should be noted that the volume of the solution increases by upstream pressure to keep the treatment duration constant at 10 min. The experiments were repeated for three times to ensure reproducible and reliable results.

In our system, under the condition even without cavitation, I_2 could still be formed by trace oxidative reactions, possibly through dissolved oxygen, resulting in the creation of trace amounts of I_2.

$$4I^- + O_2 + 2H_2O \rightarrow 2I_2 + 4OH^-$$

$$I_2 + I^- \rightarrow I_3^-$$

In the course of this work, to establish the impact of cavitation on the

Table 1
Geometrical parameters of the microscale HC reactors (see also Fig. 2 for clarity).

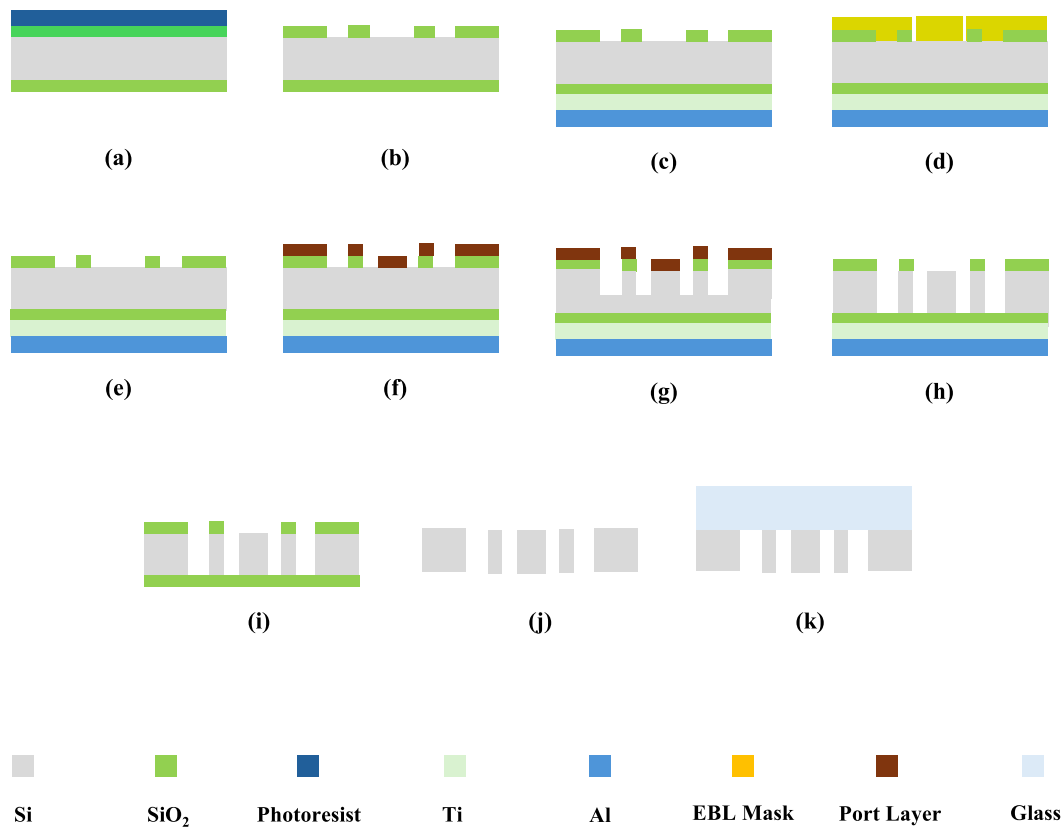| Design parameters	Definition	Reactor 1	Reactor 2
L1	Inlet channel length	3955 μm	3000 μm
L2	Nozzle length	90 μm	2000 μm
L3	Extension channel length	3955 μm	3000 μm
D	Depth	60 μm	60 μm
W1	Inlet channel width	900 μm	2100 μm
W2	Nozzle width	200 μm	700 μm
W3	Extension channel width	900 μm	2100 μm
D_h	Nozzle hydraulic diameter	92.30 μm	110.53 μm

Fig. 1. Fabrication process flow of the microscale HC reactor, a) photoresist casting on a 500 nm SiO$_2$-coated wafer, b) Etching of SiO$_2$ layer and stripping of the photoresist, c) 10 nm of Ti and 1 μm of Al sputtering on the backside of the wafer to increase the wafer durability, d) EBL mask application to define high-resolution microchannel patterns on the Si substrate, enabling precise control over channel dimensions, e) Etching of Si using the EBL-defined mask to etch microchannels with exact depth and profile, f) Lithography for the fabrication of the ports, g) Etching of Si, h) Photoresist stripping and wet etching and second etching to open inlets, outlets, and pressure ports, i) Wet etching for the removal of Al and Ti, j) Wet etching of SiO$_2$ layer, k) Anodic bonding of the Si and glass wafers.
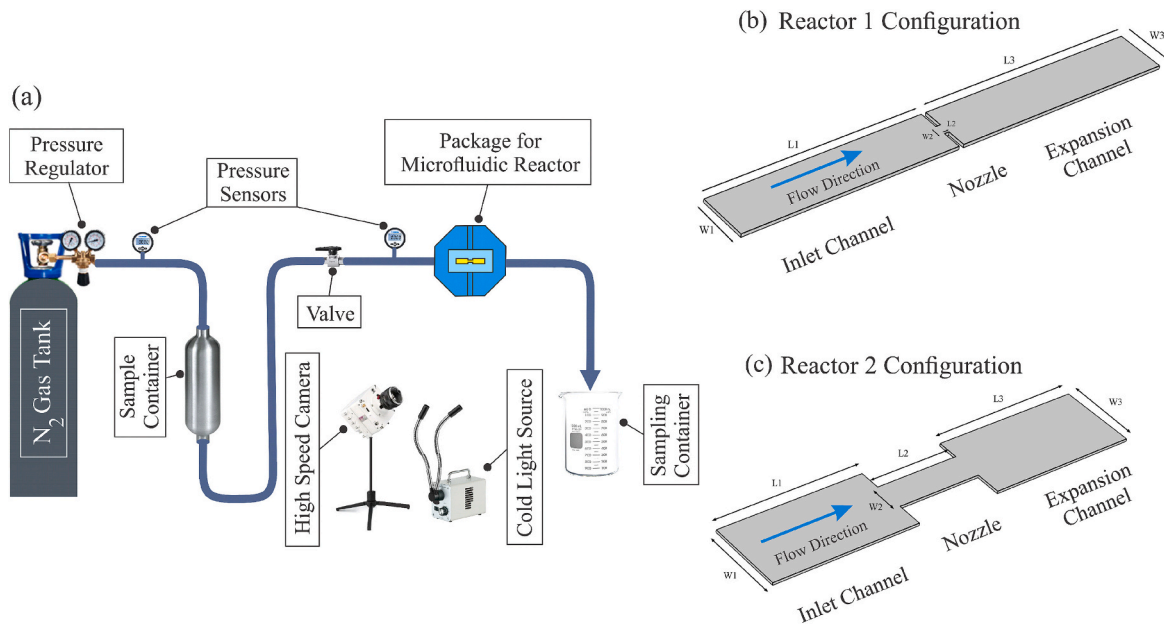

Fig. 2. Schematic of the (a) experimental setup, and (b) Reactor 1 configuration, and (c) Reactor 2 configuration (*L1*: Inlet channel length, *W1*: Inlet channel width, *L2*: Nozzle length, *W2*: Nozzle width, *L3*: Extension channel length, *W3*: Extension channel width).

Table 2
The experimental conditions for both reactors and cavitating flow patterns.

Flow pattern	Reactor 1		Reactor 2	
	Pressure (MPa)	Solution volume (mL)	Pressure (MPa)	Solution volume (mL)
Inception	0.52	120	1.03	700
Developed	1.24	220	2.07	1000
Super-cavitation	2.9	320	2.9	1300

triiodide formation, we employed the determination of the absorbance of the solution in the presence and absence of cavitation.
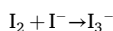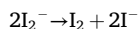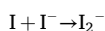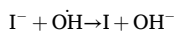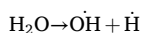
2.4. Characterization methods

2.4.1. High speed visualization of cavitating flows inside the microscale HC reactor

The HC phenomenon in the microscale HC reactor was visualized with a high-speed camera to capture high-speed fluid flow recordings. During HC inception and cavitating flow evolution, the fluid flow speed can typically exceed 40 m/s, which requires a high frame rate. To capture the flow images, a high-speed camera with a double-shutter CMOS sensor (Phantom VEO-710) was employed. The images were recorded under a range of conditions, between 7500 and 24,000 frames per second (fps) with resolutions of 1280×800 to 512×512 pixels, respectively. The camera was equipped with a macro- lens (type K_2 DistaMax) featuring a focal length of 50 mm and a f-number of 1.2. This allowed for detailed zooming during visualization. A cold light halogen source (SOIF 5100-L) was positioned at the front of the microscale HC reactor to provide the required background illumination during image acquisition.

2.4.2. UV–Vis spectroscopy and analysis procedure

In KI dosimetry, KI initially present in the solution subjected to HC, and the •OH generated from dissociation of water react with iodide ions (I^-) from the KI leading to formation of iodine radicals I_2^- and I_3^-. The main reactions occurring in this method are shown below [33]:

$$H_2O \rightarrow \dot{O}H + \dot{H}$$

$$I^- + \dot{O}H \rightarrow I + OH^-$$

$$I + I^- \rightarrow I_2^-$$

$$2I_2^- \rightarrow I_2 + 2I^-$$

$$I_2 + I^- \rightarrow I_3^-$$

The formation of I_3^- was used as an indicator of •OH production. UV–Vis analysis required approximately 2.5 min, and sampling at minutes 4 and 8 allowed immediate remeasurement of the absorbance after each UV–Vis analysis. This approach ensured at least two samples per cycle, providing sufficient data for accurate analysis. The absorbance of collected samples was measured using the UV–Vis spectroscopy (at wavelength around 353 nm [51]), providing valuable information about •OH formed during HC bubble collapse. Before each experiment, the initial absorbance value of the mixed (untreated and No Cavitation condition) *0.1 M* KI solution was also measured. The Beer-Lambert Law was used to calculate the I_3^- concentration (g/L) in the sample.

$$A = \epsilon \cdot c \cdot l \tag{1}$$

Here, *A* is the absorbance, ϵ is the molar absorptivity, *c* is the concentration of the solution, and *l* is the path length of the cuvette (1 cm). To calculate ϵ, several I_3^- solutions of known concentrations (*0.1 M, 0.5 M, 1 M*) were prepared, and their absorbances were measured with a UV–Vis spectrophotometer at the I_3^- peak wavelength. Absorbance values were plotted against concentration (with a path length of 1 cm).

The molar absorptivity (ϵ) of I_3^- at the wavelength of 353 nm was calculated from the slope of the linear relationship between absorbance (*A*) and concentration (*c*) of the solution and was found to be 26,200 M^{-1} cm^{-1} [32].

2.5. Evaluation of mixing speed and KI concentration

We focused on the role of HC on the •OH production, therefore, the effects of parameters such as mixing and KI concentrations were suppressed. The use of higher KI concentrations might lead to oversaturation or disrupt the detection process by altering the chemical equilibrium, thereby reducing the sensitivity to •OH detection. To ensure complete dissolution and exclude the impact of stirring rates on the results obtained from HC treatment, the *0.1 M* KI solution was mixed at three different rating speeds (50, 100, and 150 rpm) until a clear solution was obtained. The solution was then immediately analyzed using UV–Vis spectroscopy. As shown in Fig. 3a, the concentration of I_3^- increased over time, with higher stirring speeds due to the enhanced mixing effect. This increase, which was observed in the absence of HC, shows the significant influence of mixing on KI reactivity. On the other hand, to investigate the effect of concentration, KI solutions with three different concentrations of *0.1 M, 0.5 M*, and *1 M* were prepared at a stirring speed of 50 rpm, which was selected according to the results of Fig. 3a (unaffected I_3^- concentration), and the solutions were analyzed using UV–Vis spectroscopy. As illustrated in Fig. 3b, the concentration of I_3^- increased with KI concentrations from *0.1 M* to *1 M*. As a result, to minimize the interference and to maintain consistent conditions during cavitation, we selected *0.1 M* KI (prepared at 50 rpm) as the standard solution for all the experiments.

3. Results and discussion

3.1. Variations of I_3^- mass concentration with respect to time and upstream pressure of HC

Fig. 4a and b represent the I_3^- mass concentration, which is the indicator for the generation of •OH measured by KI dosimetry for Reactor 1 and Reactor 2, with respect to upstream pressure and time.

I_3^- formation for Reactor 1 increases to a maximum value at the pressure of 0.52 MPa (Fig. 4a) beyond which it decreases until a plateau value. The sharper drop in I_3^- formation observed in Reactor 1, as compared to Reactor 2, is primarily attributed to differences in the flow pattern through the micro-orifice. In Reactor 1, there is insufficient length for bubble formation within the nozzle itself. As a result, cavitation phenomena—including shear-layer vorticities and cavity shedding—occur predominantly in the extension channel, leading to a more abrupt pressure drop (see Fig. 5). In contrast, the longer nozzle geometry of Reactor 2 allows a separated bubble to form within the channel, enabling more effective pressure recovery before flow enters the extension channel. This additional recovery step mitigates the pressure drop and thus produces a less pronounced decline in I_3^- formation (see Fig. 4a). After this pressure, the I_3^- formation is approximately the same by increasing the pressure. The I_3^- formation for Reactor 2 increases up to around 2.07 MPa and after this pressure, the changes in I_3^- production are negligible. Accordingly, the maximum concentration of I_3^- for Reactor 1 occurs at a pressure of 0.52 MPa, whereas for Reactor 2, this pressure is around 2.07 MPa (Fig. 4a). The results show that the maximum I_3^- production in Reactor 1 is approximately 30 % higher than that of Reactor 2. The cavitating flow patterns for these configurations and at the prescribed upstream pressures vary dramatically. This variation is depicted in the level of the I_3^- formation as an indicator of •OH necessitating the need for in-depth investigation of the relationship between the cavity dynamics and chemical effects of the HC bubble collapse. Fig. 4b illustrates the changes in I_3^- production over time under three conditions: untreated (mixing without HC process), passing through Reactor 1 and Reactor 2. This figure shows that I_3^- production
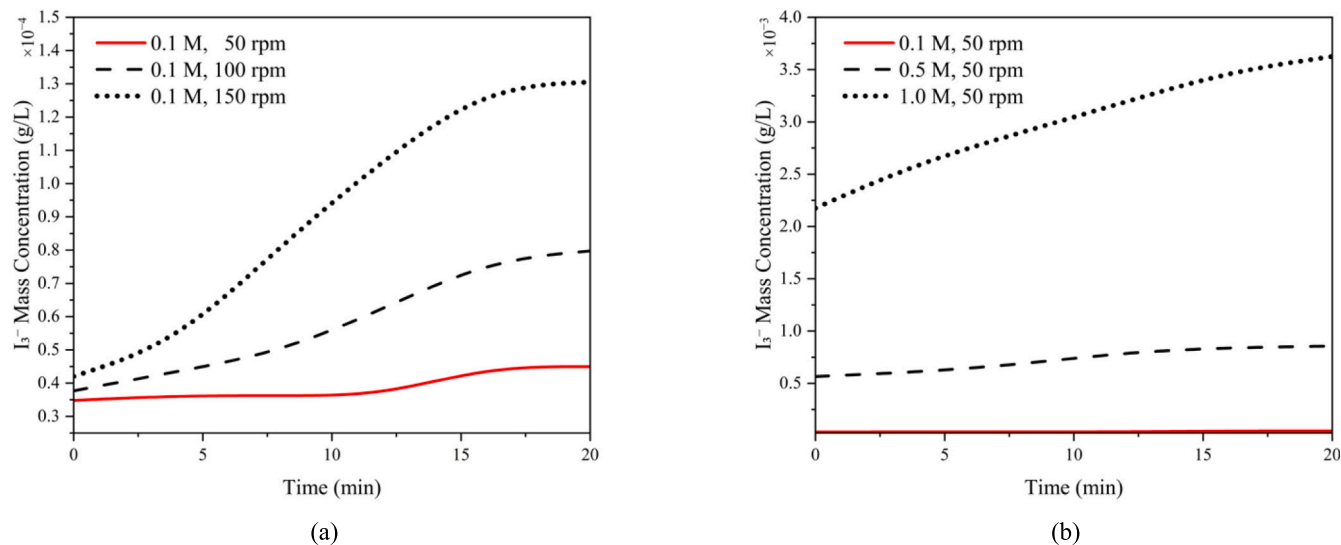
(a)

(b)

Fig. 3. (a) I_3^- variation over time at different mixing speeds (rpm) and (b) I_3^- variation over time at different KI concentrations.
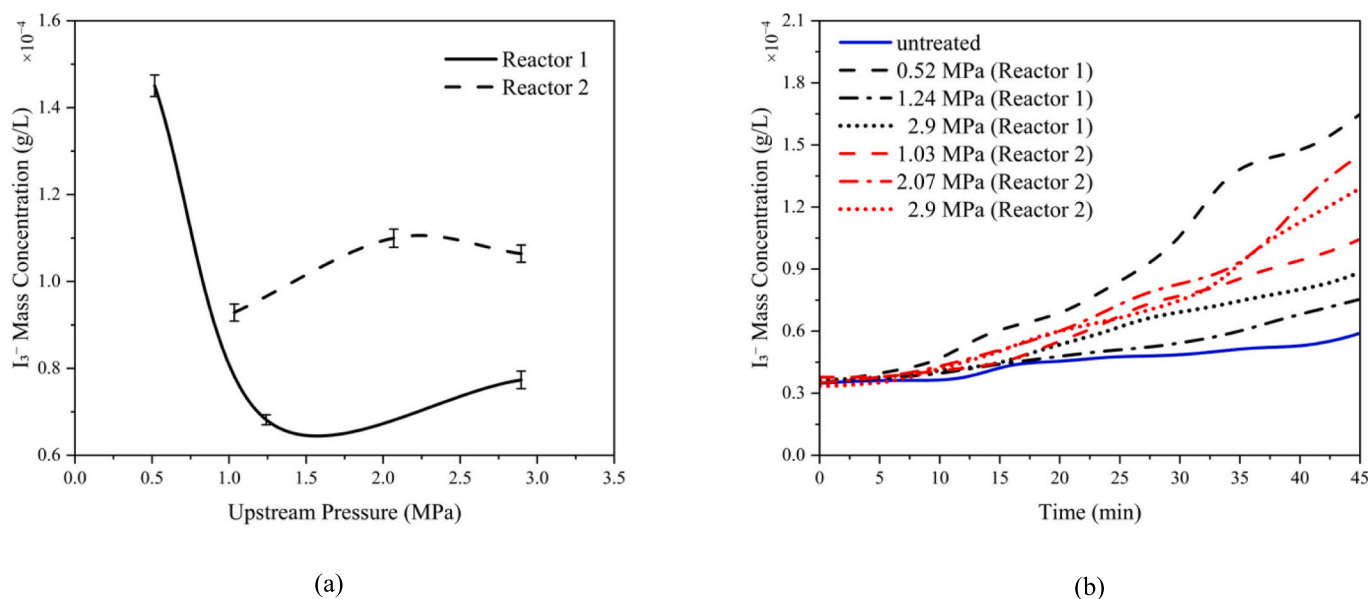

(a)

(b)

Fig. 4. (a) Pressure-dependent I_3^- formation in Reactor 1 and Reactor 2 and (b) time-dependent I_3^- formation in Reactor 1 and Reactor 2 (The effect of the mixing prior to HC was also considered in all graphs. Error bars represent the standard error of three independent replicates, n = 3.)

increases over time, although this increase is dependent on both the pressure and type of reactor.

The results confirm that the production of I_3^- is higher for the HC treated cases, regardless of the reactor, compared to the untreated case. Furthermore, when comparing three different upstream pressures for Reactor 1, it can be observed that the highest I_3^- production occurs at the pressure of 0.52 MPa, with a production rate that increases over time. In Reactor 2, however, an increase in both pressure and time results in a rise in I_3^- production, with the highest production rate observed at the pressure of 2.07 MPa. The comparison between Reactor 1 and Reactor 2 reveals an interesting trend for I_3^- production according to the cavitating flow pattern, upstream pressure and time of HC process. It is shown that a facile chemical effect of the microscale HC bubble collapse could be achieved even at a low upstream pressure (0.52 MPa) for Reactor 1, while less I_3^- production is attained at a high upstream pressure (2.9 MPa) for Reactor 2.

3.2. Cavitating flow patterns inside the microscale HC reactor

Fig. 5 shows the high-speed camera images indicating the major cavitating flow patterns within Reactor 1 for three upstream pressures of 0.52 MPa, 1.24 MPa, and 2.9 MPa. In each of the schematics shown, the transition is given through three main flow patterns of inception, developed, and super-cavitation condition.

The flow pattern in Reactor 1 at the pressure of 0.52 MPa is the incipient cavitating flow, wherein vapor formation initiates due to a local reduction in the pressure at the nozzle inlet. A detachment flow separation at the sudden contraction causes twin attached cavity formations along the walls downstream of the nozzle as shown in Fig. 5a. These cavities remain stabilized within the developing shear layer, which forms between the high-velocity jet flow and adjacent recirculation zones [52]. The Reynolds number, which is measured as $Re = \rho v D_h / \mu$ (where ρ, v, D_h, and μ are the liquid density, flow mean velocity, hydraulic diameter and viscosity, respectively) is about 3000 for this pressure, indicating a transitional regime of flow (Fig. 5a). To calculate
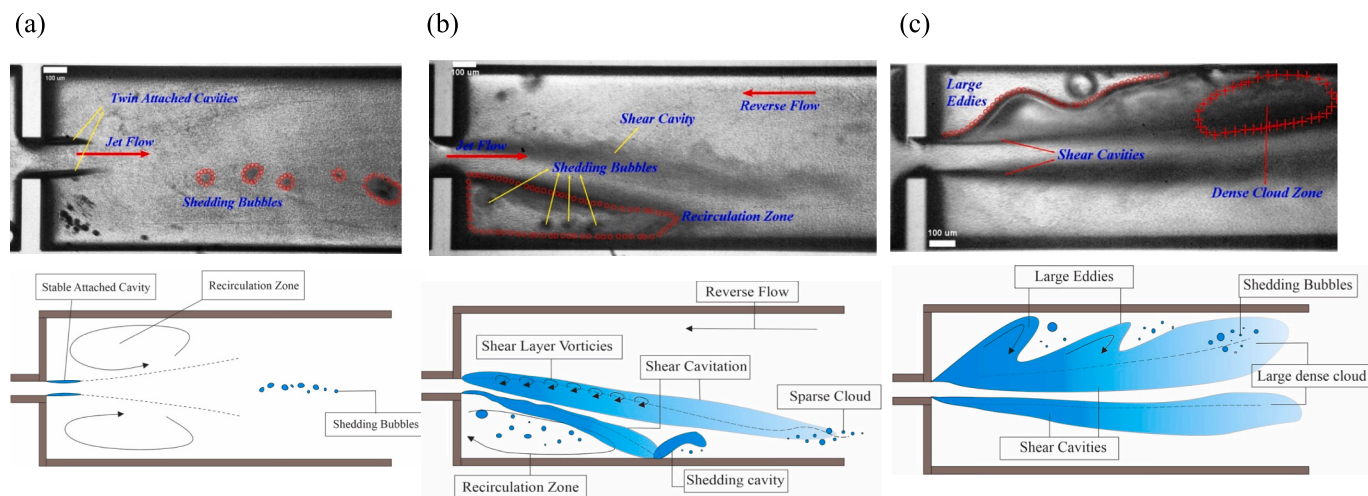
(a)   (b)   (c)

Fig. 5. Cavitating flow patterns within Reactor 1 at upstream pressures of (a) 0.52 MPa, (b) 1.24 MPa, and (c) 2.9 MPa. Up: High-speed camera visualization, and Down: Flow pattern schematics (blue color indicate HC bubbly and cloud formations). (For interpretation of the references to color in this figure legend, the reader is referred to the web version of this article.)

the mean velocity, the flow rate is calculated for a specific volume and time of HC process ($Q = V/t$). In this equation, Q represents the flow rate in units of L/s, V denotes the volume of the graduated cylinder in liters (L), and t indicates the time in seconds (s). Subsequently, based on the equation $Q = Av$, where A is the nozzle cross-sectional area of Reactor 1 or Reactor 2, the velocity v could be calculated. In this regime, instabilities created by the vortex shedding, which are developed in the shear layer, promote bubble detachment while triggering cavitation inception but preserving flow coherence—a characteristic of the incipient cavitating flow.

Further downstream, shedding bubbles can be seen intermittently (Fig. 5a), which shows that the transition toward a more developed cavitating flow pattern could be happened upon excessive pressure drop in the nozzle. This behavior agrees with the observations of cavitation in microfluidic reactors, where shear layer dynamics, flow separation, and pressure recovery play critical roles in cavitation inception and bubble dynamics [20]. At the pressure of 0.52 MPa, cavitation inception not only represents the onset of bubble formation but also promotes the collapse of small bubbles, which produces intense local pressure peaks [53,54]. Such a violent collapse could effectively dissociate water molecules to form •OH and other reactive intermediates. Moreover, the repeated growth and collapse of the cavitation bubbles in this regime dynamically changes the flow field surrounding them, thereby modifying the local pressures, which further causes oscillations in the bubble volume. These oscillations interact with the strong variations in velocities and pressures during bubble collapse, enhancing instabilities in the flow field. These enhanced instabilities not only affect the flow structure but also promote interactions between radicals and target molecules such as persistent organic pollutants (POPs), pharmaceuticals, or industrial dyes, thereby amplifying the chemical effects [55].

At the pressure of 1.24 MPa, the Reynolds number is approximately 4900 and the developed cavitating flow pattern is characterized by intense vapor generation (Fig. 5b). At this Reynolds number, the fully turbulent nature of the flow enhances vortex shedding and promotes interactions among the shear layer, recirculation zone, and reverse flow, resulting in high cavitation intensity [56]. The sharp pressure drops at the nozzle exit induces shear cavitating flow along the shear layer, which forms at the interface between the high-velocity jet flow and surrounding fluid. Coherent vortices develop within this shear layer and low-pressure cores that sustain vapor phase growth. As the penetration of cavitating flow progresses, shedding cavities periodically detach from the shear layer. This detachment is strongly influenced by the re-entrant jets and shockwave propagation due to sparse vapor clouds collapse

downstream of the extension channel [57]. Below the jet flow, a well-defined recirculation zone develops due to flow separation and acts as a reservoir for vapor nuclei and contributes to bubble stabilization while promoting turbulence in the flow field [58,59]. At the same time, a reverse flow region forms at the upper boundary due to the adverse pressure gradient. The flow behavior mentioned above aligns with the observations regarding microfluidic reactors in the literature, where shear layer dynamics, flow separation, and turbulence intensification play a key role in sustaining cloud cavitation and periodic bubble detachment [56,58,60,61].

At the pressure of 2.9 MPa, the Reynolds number is approximately 8000 and the super-cavitation condition could be seen in Reactor 1, where there is a continuous shear cavity occupying a large portion of the channel due to the sharp pressure drop across the nozzle (Fig. 5c). The elongated shear cavities develop along the shear layer due to Kelvin-Helmholtz instabilities produced by the velocity gradient between the high-speed jet flow and the surrounding fluid, leading to large-scale eddies [58]. These eddies have low-pressure cores, sustaining vapor phase formation and further enhancing cavity elongation. Further downstream, the shear cavity collapses in a dense cloud zone, where vapor bubbles condense due to pressure recovery in the expansion region, induce localized high-pressure waves, and contribute to flow destabilization. Large-scale eddies at the vapor cloud boundary, as seen in Fig. 5c, indicate the turbulent interactions with the ambient fluid, further stabilizing the flow and reducing the occurrence of violent vapor collapses. Beyond this zone, shedding bubbles detach intermittently as the shear layer becomes unstable under turbulent flow conditions [57]. In this regime, large and stable vapor bubbles extend far downstream of the nozzle, completely dominating the flow and drastically changing cavitation dynamics. Stabilization of the cavity shape implies the flattening behavior of the •OH production due to energy transfer shifting from localized bubble collapses to a more stable cavity shape.

Our results show that while shear cavities still form at the interface between the high-velocity jet and slower surrounding fluid, their contribution to chemical effects becomes negligible compared to the dominant influence of the large, stable vapor cloud. The super-cavitation condition therefore represents a shift, where turbulence and cavity stabilization limit chemical activity, aligning with the observed stabilization of •OH concentration [60–62]. This flow physics arises from the balance among shear instabilities, redistribution of energy, and flow stabilization at high Reynolds numbers associated with microfluidic systems [63,64].

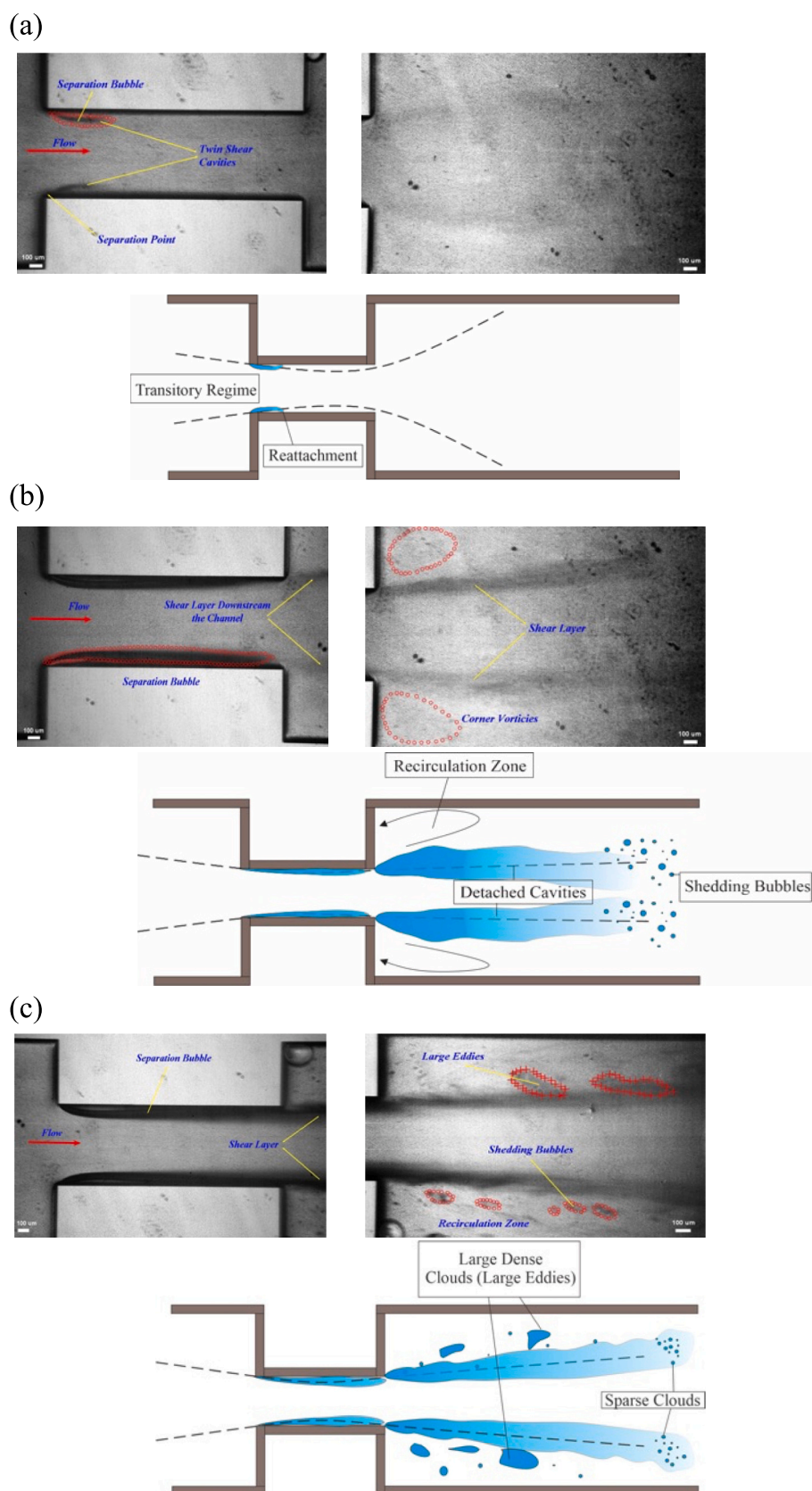The flow pattern showed in Fig. 6 illustrates the evolution of

Fig. 6. Cavitating flow patterns within Reactor 2 at upstream pressures of (a) 1.03 MPa, (b) 2.07 MPa, and (c) 2.9 MPa, Top left: High-speed visualization inside the nozzle, Top Right: High-speed visualization in the extension channel, and Bottom: Flow pattern schematics (blue color indicates HC bubbly and cloud formations). (For interpretation of the references to color in this figure legend, the reader is referred to the web version of this article.)

cavitating flow patterns in Reactor 2 at different upstream pressures, from 1.03 to 2.9 MPa. At the pressure of 1.03 MPa, the Reynolds number is approximately 13,000, and the flow inside Reactor 2 corresponds to the incipient cavitating flow. It should be noted that cavitation bubbles first appeared in this reactor at a relatively higher upstream pressure (1.03 MPa) compared to Reactor 1 (0.52 MPa). At the pressure of 1.03 MPa (Fig. 6a), cavitation initiates with small bubble clusters forming along the channel walls, leading to I_3^- production and •OH generation through localized chemical reactions [65]. There is not any cavitation activity recorded in the extension channel at this pressure, which could limit the chemical effects activity in the inception flow for this reactor. In this regime, early cavitation bubbles are developed due to the localized pressure drop near flow separation points. The flow separates at the sharp contraction (nozzle) of the diaphragm, giving rise to a separation bubble at the nozzle inlet. In the wake, on either side of the separation point, a pair of shear cavities develop along the shear layers between the high-velocity jet flow and surrounding slower fluid. These are sustained by low-pressure zones, which are generated by shear layer instabilities [52]. These shear layer instabilities become enhanced in the turbulent flow due to the Reynolds number of 13,000, enhancing local nucleation of cavitation but limiting the growth of the bubbles due to the short residence time [20]. Downstream of this region, the flow starts to attach to the diaphragm walls, initiating the transition to a more stable flow known as the transitory regime, where the pressure recovery limits the vapor formation and stabilizes the flow [66].

At the pressure of 2.07 MPa, the Reynolds number is about 19,500, and the flow corresponds to the developed cavitating flow pattern characterized by sheet cavity formation and further detachment by shear layer instabilities. The flow separates at the sharp edges of the nozzle with a low-pressure region which forms to sustain the growth of elongated sheet cavities along the diaphragm walls [63]. The expansion in the extension channel generates shear layer instabilities between the high-velocity jet flow and surrounding fluid, destabilizing and detaching the vapor cavities. Further downstream, the detached cavity breaks into shedding bubbles, which collapse violently under the influence of pressure recovery [57]. At this Reynolds number, the flow is highly turbulent, and shear layer instabilities are significantly enhanced, promoting corner vortices and recirculation zones to form at the channel boundaries. These recirculation zones serve as reservoirs for vapor nuclei and interact with detached cavities, enhancing the frequency of cavitation cloud shedding [67–69]. Thus, this regime results in periodic high-intensity collapses with corresponding localized pressure and temperature jumps, typical of fully developed cavitating flow. The flow morphology highlights the critical roles of the shear layer, turbulence, and recirculation zones in creating highly nonlinear flow structures, which are essential in establishing a developed cavitating flow pattern at high Reynolds numbers in microfluidic environments [59,70]. Consequently, as reflected in Fig. 4a, the flow morphology and dynamics significantly enhance the formation of I_3^- and boost production of •OH.

At the pressure of 2.9 MPa, the flow within Reactor 2 transitions shows the super-cavitation condition (Fig. 6c). In the nozzle, the flow separation and significant pressure drop induce the formation of sheet cavities along the diaphragm walls, facilitating vapor generation in regions with low static pressure. As the flow proceeds to the extension channel, the shear layer becomes unstable and large eddies form due to Kelvin-Helmholtz instabilities at the interface of the high-velocity jet flow and surrounding fluid [58]. These eddies disrupt the vapor interface, thereby promoting the growth of dense vapor clouds which expand and fill the downstream channel [52]. Eventually, these dense clouds break-down under the influence of the pressure recovery and turbulent flow conditions into sparse vapor clouds and shedding bubbles. Besides, the existence of recirculation zones along the channel walls leads to the stabilization of vapor pockets and enhanced turbulence-driven interactions within the flow [66]. The corresponding Reynolds number is 25,000, and the fully turbulent flow amplifies shear layer instabilities and eddy formation, leading to periodic vapor detachment and

continuous breakdown of vapor clouds. This interplay among shear instabilities, turbulence, and recirculation effects maintains the supercavitation pattern, where large-scale vapor cavities prevail in the flow [56]. This behavior explains the gradual response of this configuration to pressure changes and its suitability for applications requiring stable cavitation and consistent •OH generation across broader pressure ranges, particularly in oxidation reactions, wastewater treatment, and disinfection processes [31,71,72]. Video recordings of the flow patterns under the inception and developed regimes for both the micro-orifice and long diaphragm reactors are available as supplementary material (Videos S1 and S2).

3.3. Cavitation number and flow rate profiles: implications for chemical reaction dynamics

The cavitation number and flow rate profiles are displayed in Fig. 7 at different upstream pressures for Reactor 1 and Reactor 2. The cavitation number provides information about the cavitation intensity in cavitating flows. The cavitation number is expressed as:

$$C_v = \frac{P_{up} - P_v}{\frac{1}{2}\rho v^2} \tag{2}$$

where P_{up}, P_v, ρ, and v are the reference pressure (the upstream pressure), vapor saturation pressure of the liquid, liquid density, and flow mean velocity, respectively. Cavitation number and flow rate profiles give insights into the differences in I_3^- production and •OH generation.

Fig. 7a shows the upstream pressure as a function of flow rate for the two reactors. The Reactor 2 has significantly higher flow rates compared to Reactor 1, with a quasi-linear variation in the flow rate with upstream pressure for both configurations. Observed differences in flow characteristics are largely attributed to the distinct geometries of the cavitation reactors, which influence the flow patterns and cavitation behavior within each reactor. At the pressure of 2.9 MPa, the flow rate reaches 2.2 mL/s for Reactor 2, while the flow rate is 0.5 mL/s for Reactor 1. The difference in flow characteristics leads to the distinctive cavitating flow behaviors, chemical effects, and •OH production as displayed in Fig. 4. In Reactor 2, the combination of its geometry and higher flow rates creates more persistent cavitation zones, which extends bubble lifetimes. These extended residence times provide more opportunities for energy transfer, enhance exposure to cavitation conditions, and promote reactions such as the decomposition of water into •OH. This longer exposure to the cavitation conditions explains the slow rise in I_3^- production and •OH with pressure in Reactor 2 until higher peaks compared to Reactor 1. The increased fluid throughput facilitates more cumulative cavitation events along the channel length, which accounts for the elevated I_3^- production and •OH formation observed at the pressure of 2.9 MPa as displayed in Fig. 4b. The lower flow rates in Reactor 1 correlate with the profound peak of I_3^- formation and •OH generation at relatively lower upstream pressures (around 0.52 MPa as shown in Fig. 4a). Similar to restricted orifice flow conditions, small, intense, and focused cavitation zones optimize chemical effects and •OH production at relatively lower pressures. This phenomenon corresponds to cavitation inception, where there is a balance between cavitation intensity and energy.

The right vertical axis of Fig. 7a illustrates the variation in the velocity with the pressure. According to this figure, in Reactor 1, velocity increases with pressure. However, beyond the pressure 1.24 MPa, the velocity gradient becomes steeper, indicating intensified shear layer instabilities and rapid bubble detachment, resulting in a dynamic cavitating flow pattern as discussed in detail in Fig. 5. In Reactor 2, the velocity also increases with pressure, but this increase is considerably higher than that in Reactor 1. This is attributed to the differences in the hydraulic diameter of the microchannels and the distinct reactor geometries, which lead to varying cavitating flow patterns and different velocity magnitudes, as elaborated in Fig. 6.

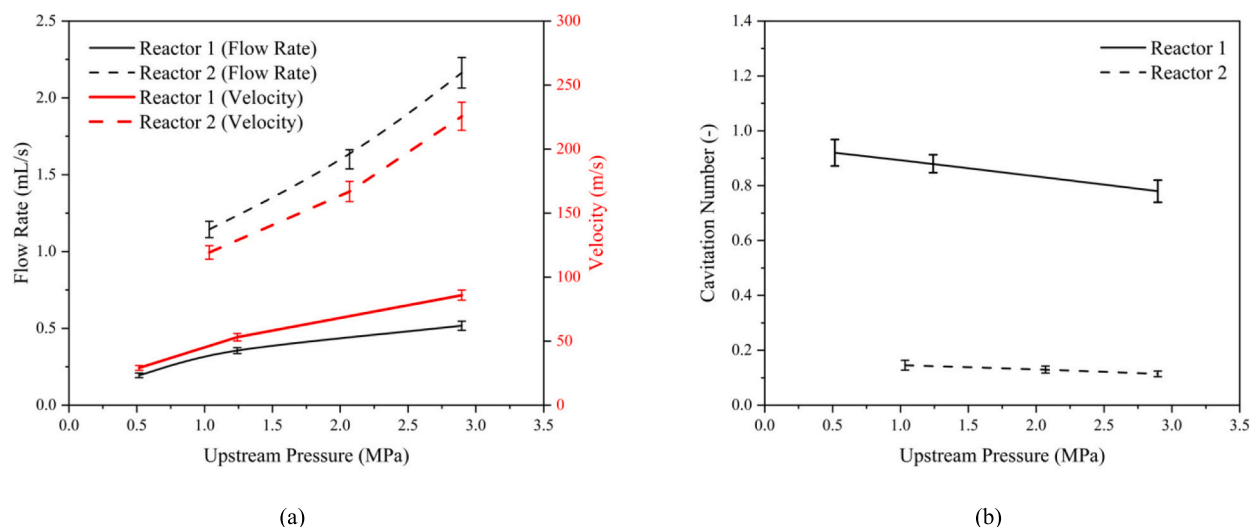As shown in Fig. 7a, the flow velocity increases with the upstream

(a)

(b)

Fig. 7. (a) Flow rate and velocity profiles for Reactor 1 and Reactor 2, and (b) Cavitation number comparisons between Reactor 1 and Reactor 2. Error bars indicate the standard error from three independent experiments (n = 3).

pressure, leading to a decrease in the cavitation number. The cavitation number remains smaller than 1 (see Fig. 7b), which is consistent with the findings in the literature [20,73,74]. Fig. 7b demonstrates the cavitation number trend for both geometries across the three cavitation regimes (inception, developed, and super-cavitation) for each reactor. The cavitation number profile of Reactor 1 agrees with intense chemical effects and generation of •OH at low pressures [75,76]. However, this trend does not linearly translate to increased production of I_3^- and •OH at higher pressures, as evidenced in Fig. 4a. This can be explained with the transition to super-cavitation condition at high pressures, around 2.9 MPa, where the formation of stable vapor cavities becomes prominent [20,71,77]. For Reactor 2, the lower Cavitation numbers suggest that the parameters, such as extended residence time, pressure recovery patterns, and the development of quasi-super-cavitation regimes, play a more dominant role in determining the overall cavitation intensity, chemical effects, and •OH production. While Reactor 1 has higher cavitation numbers, the large flow rates and cavitation regimes for Reactor 2 allow for enhanced cumulative chemical effects and sustained •OH production, particularly at higher pressures and over extended periods.

It should be noted that the sudden expansion and steep local pressure drop of the fluid through Reactor 1 make conditions very favorable for the formation and collapse of cavitation bubbles even at lower flow rates, and thus, intense but localized •OH production is possible. In contrast, the extended geometry of Reactor 2 combined with higher flow rates leads to a more distributed cavitation effect, so that it likely promotes more sustained chemical activity over time, enhancing the overall radical generation.

3.4. Power consumption and cavitation yield: implications for efficiency, economics, and •OH production

The hydraulic power delivered to the liquid by HC is determined using the pressure provided by the nitrogen tank, which is the only energy source for such a system, driving the fluid flow through the piping and inducing the HC phenomenon. The hydraulic power is given as, $Power = P_{up} \cdot Q$, where Q is the flow rate, P_{up} is the upstream pressure introduced by the nitrogen tank, and $Power$ is in W.

Power consumption and cavitation yield provide important information about the efficiency and effectiveness of reactors (displayed in
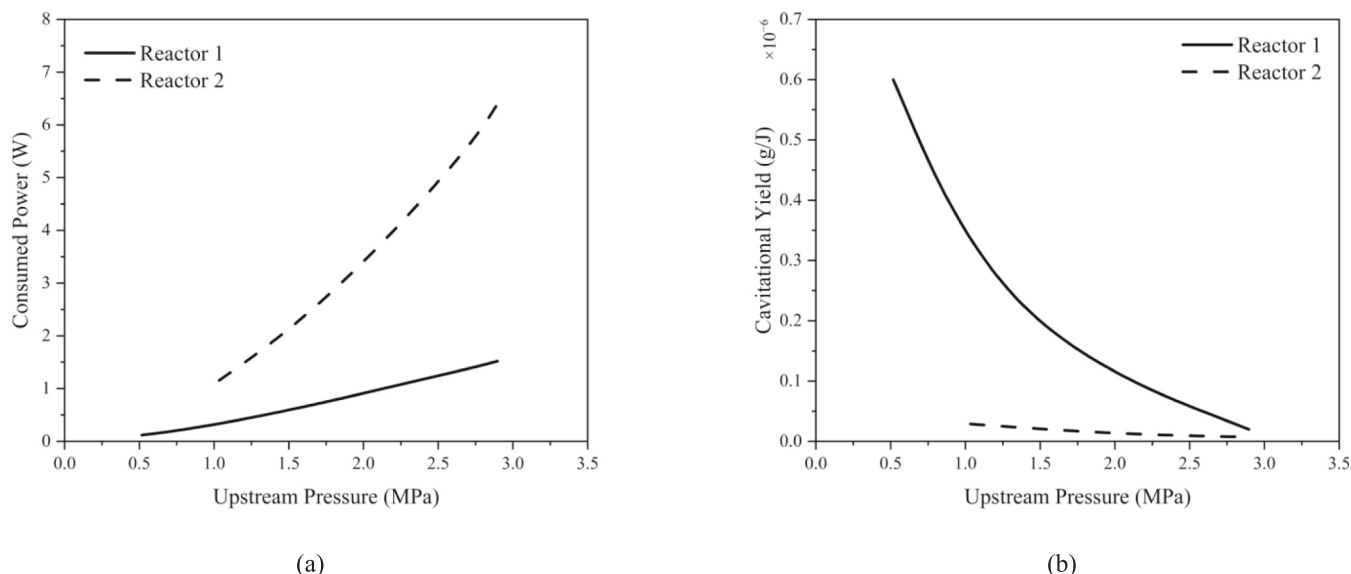

(a)

(b)

Fig. 8. (a) Power consumption and (b) Cavitational yield as a function of upstream pressure for Reactor 1 and Reactor 2.

Fig. 8a and b, for Reactor 1 and Reactor 2, respectively). These parameters are of paramount importance in determining the energy input, chemical effects and •OH production relationship in microscale HC reactors. The cavitational yield is an indicator of the efficiency of the HC system, which is measured through the desired product formed versus the amount of energy introduced. The cavitational yield can, thus, be defined as the ratio of the produced I_3^- to the consumed energy by the system at upstream pressures:

$$\text{Cavitational yield} = \frac{\text{Mass of I3}^- \text{produced (g)}}{\text{Energy input (J)}} \qquad (3)$$

This yield is a very important parameter in the estimation of the chemical performance of HC systems, as it reflects how well the input energy is converted into the desired chemical changes via cavitation.

As seen in Fig. 8a, the power consumption increases with the upstream pressure for both configurations. However, the rate of increase is significantly higher for Reactor 2 configuration compared to Reactor 1. For instance, at the pressure of 2.9 MPa, Reactor 2 consumes approximately 6.4 W, compared to just 1.5 W corresponding to Reactor 1. This difference stems from the larger flow rates required by the long micro-diaphragm, which results in larger energy demands. The steeper power consumption trend for Reactor 2 highlights its energy-intensive nature, which can be attributed to the fundamental differences in flow characteristics between the two configurations. This difference in power consumption agrees with the differences in the flow rate shown in Fig. 7a. Accordingly, larger flow rates in Reactor 2 require larger energy and hence more power consumption. The differences in power consumption can be explained by the fundamental differences in flow characteristics of the two configurations discussed in the previous section. Fig. 8b shows the cavitational yield as a function of the upstream pressure, with the observed trends inversely related to power consumption. Reactor 1 configuration leads to considerably higher cavitational yields within the entire pressure range compared to Reactor 2. At lower pressures (around 0.52 MPa), Reactor 1 achieves the maximum cavitational yield of about 0.6×10^{-6} g/J, while Reactor 2 peak is at 3.0×10^{-8} g/J at 1.03 MPa (the cavitation inception pressures for both Reactors). This peak in cavitational yield for Reactor 1 supports the link between cavitational yield and previously discussed chemical effects. Interestingly, the cavitational yields for both configurations decrease at higher pressures, likely due to the transition into the super-cavitation regime, where excessive bubble formation and vapor cavity stabilization reduce the intensity of localized collapse events. Despite this reduction, Reactor 1 consistently outperforms Reactor 2, highlighting its efficiency in energy utilization for radical generation and I_3^- production. The relationship among power, yield, and cost is represented as the Cost parameter expressed as:

Fig. 9. Economic analysis of microscale HC reactors.

Reactor 2. In contrast, for Reactor 2 configuration, the maximum I_3^- production is achieved at developed regime (2.07 MPa). However, the energy cost at this pressure is approximately 98 % higher than the cost at the optimal I_3^- production condition in Reactor 1 (0.52 MPa). The economic analysis highlights that, for cost-effective I_3^- production, the operation of Reactor 1 at inception represents the most optimal scenario among the tested pressures and reactor configurations. These disparities underscore the significant cost advantages of operating Reactor 1 under optimal conditions.

While Reactor 2 provides a more uniform •OH distribution along its length due to its broader cavitation zones and extended flow paths, this benefit comes at the expense of excessive power consumption, particularly at higher pressures. For example, at the pressure of 2.9 MPa, Reactor 2 consumes more than four times power compared to Reactor 1 while achieving a lower cavitational yield. This trade-off should be carefully considered when selecting the microscale HC reactor configuration for a specific application.

3.5. Comparison between microscale and macroscale HC reactors: advantages of "HC on a Chip" concept for enhanced •OH production

In order to highlight the performance of the microscale HC reactors, we compared the performance of the micro-orifice and the long diaphragm reactors with two macroscale plate designs previously tested by

$$\text{Cost} = \frac{\text{Power consumption (W)} \times \text{Operating time (s)} \times \text{Energy price (USD/kWh)}}{\text{Cavitational yield (g/J)} \times \text{Energy input (J)}} \qquad (4)$$

The economic analysis with this parameter is based on the actual electrical energy consumed during each process, with the electricity cost set at 0.047 USD/kWh [78] (as presented in Fig. 9).

As illustrated in Fig. 9, energy consumption costs increase with the pressure for both reactors as the cavitating flow pattern shifts from inception to super-cavitation (i.e., with increasing pressure), which is an expected outcome. However, a key finding of this study is that the maximum production of I_3^- in Reactor 1 configuration occurs at inception (equivalent to 0.52 MPa). Notably, this pressure also corresponds to the lowest energy cost among all tested pressures and even compared to
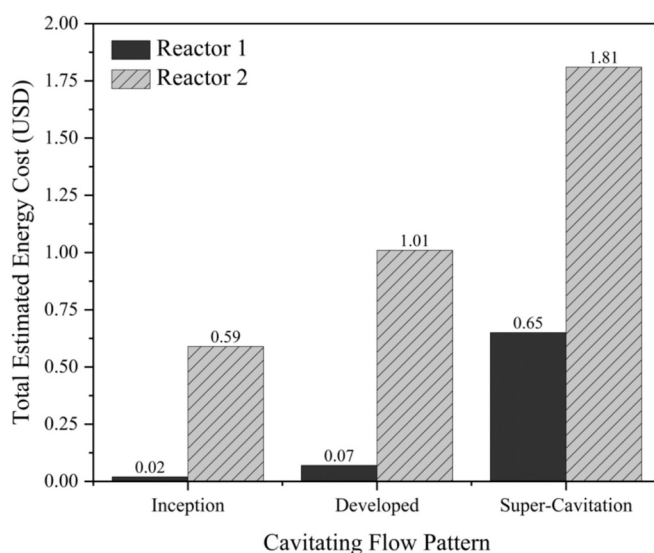
Kumar et al. [79]. The results obtained from the KI test (Fig. 4a) showed that, for Reactor 1, the highest I_3^- production—and thus the strongest chemical effect of cavitation—occurs at 0.52 MPa, which is the pressure required for cavitation inception. In contrast, for Reactor 2, this maximum occurs at 2.07 MPa. To compare micro-scale and macro-scale effects, the production and rate of I_3^- in the micro reactors are compared with [79], where 0.35 MPa corresponds to the highest I_3^- production. These comparisons were made based on I_3^- production as a function of cavitation intensity and •OH generation, represented in terms of both concentration-time profiles and reaction rates-time profiles (Fig. 10).

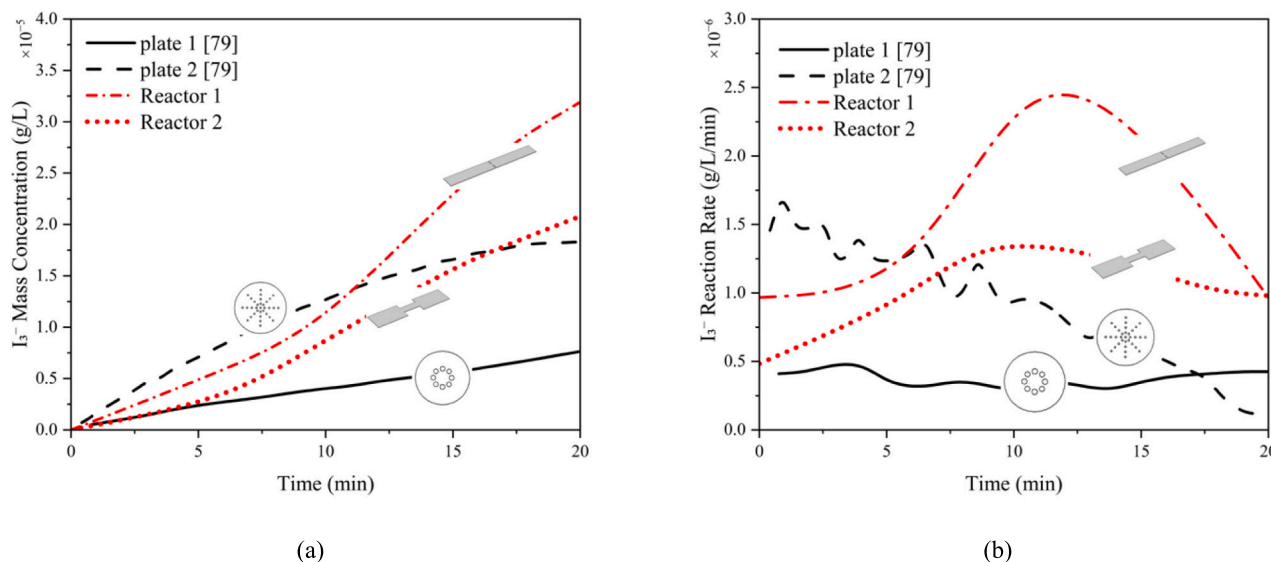Plate 1, as shown in Fig. 10, had 8 holes of 5 mm diameter in a

(a)

(b)

Fig. 10. (a) I_3^- mass concentration and (b) I_3^- reaction rate as a function of time for Reactor 1 at 0.52 MPa and Reactor 2 at 2.07 MPa and two macroscale plate configurations at 0.35 MPa [79].

circular pattern, while Plate 2 contain 33 holes of the same diameter in a star-like pattern. Besides the difference in the number of holes, the pattern also influence performance, with Plate 2 consistently out-performs Plate 1 in terms of I_3^- production and generating more $\cdot$OH.

Fig. 10a presents the first 20 min of our experiments together with the results obtained from a macroscale reactor (Kumar et al. [79]) for I_3^- production. In this graph, the effect of the mixing (3.5×10^{-5} g/L of I_3^-) is excluded from our results to enable a fair comparison between the datasets. Consequently, our data were shifted downward by 3.5×10^{-5} g/L so that both start from the same initial point. Within a 20-minute observation period, Reactor 1 achieves the highest final concentration of approximately 3.2×10^{-5} g/L, followed by Reactor 2 (2.1×10^{-5} g/L). Although cavitation conditions (e.g., pressure, flow rate, geometry) were constant, the reaction rate rose during the first ~10 min, then declined. Over time, the increased bubble interactions reduce $\cdot$OH availability and collapse energy, lowering radical generation efficiency, as noted by Yasui et al. and Stricker et al. [80,81]. Plate 2 and Plate 1 reach the concentrations of 1.85×10^{-5} g/L and 0.8×10^{-5} g/L, respectively. Reactor 1 exhibits a distinctive pattern of an initial rapid increase in I_3^- production followed by a gradual but sustained rise, which is indicative of continuous cavitation activity and sustained $\cdot$OH production. Similarly, Reactor 2 displays a nearly steady and consistent increase in I_3^- concentration over time, suggesting prolonged and effective cavitation conditions. In contrast, both plate designs have a plateau-shaped trend. Plate 2 has a trend leveling off after approximately 15 min while Plate 1 has a slower, linear increase. These trends highlight the superiority of microfluidic reactors in maintaining sustained $\cdot$OH production.

The reaction rate profiles shown in Fig. 10b further illustrate the dynamic nature of cavitation processes for these four configurations as below:

1. Reactor 1: The reaction rate increases during the initial 12 min, reaching a peak of approximately 2.45×10^{-6} g/L per minute, after 12 min, the rate declines to about 1.0×10^{-6} g/L per minute by 20 min. The observed decline in reaction rate is likely due to increased bubble-bubble interactions as cavitation intensifies. These interactions can cause shielding influences and can reduce collapse symmetry, which can restrict radical generation efficiency [80,81].
2. Reactor 2: The reaction rate increases steadily, reaching 1.4×10^{-6} g/L per minute at its maximum (first 10 min) and then decreases to 1.0×10^{-6} g/L/min at the end of the test. The geometry of Reactor 2
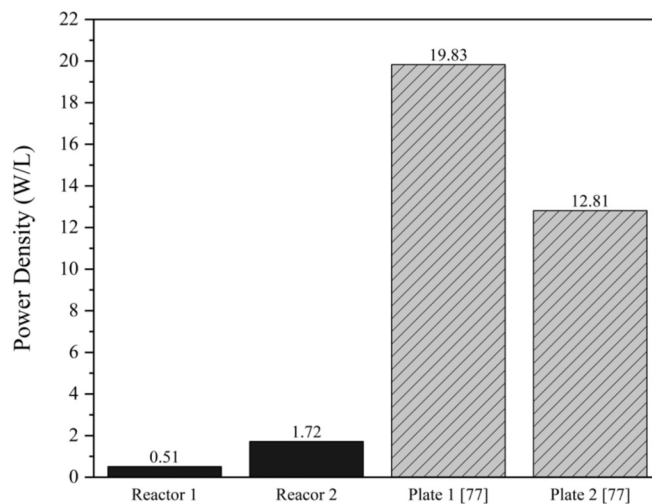

Fig. 11. Power density for Reactor 1 (at 0.52 MPa) and Reactor 2 (at 2.07 MPa) and two macroscale plate configurations (at 0.35 MPa) [79].

supports broader cavitation zones and uniform flow, leading to consistent cavitation activity.
3. Plate 1 (macro-scale): The reaction rate remains relatively stable at approximately 4.0×10^{-7} g/L/min, reflecting minimal cavitation intensity and lower efficiency in generating reactive species. This uniform but low performance aligns with its simpler design, which lacks the ability to generate intense localized cavitation.
4. Plate 2 (macro-scale): It initially has the highest reaction rate among the plate configurations, reaching 1.6×10^{-6} g/L/min within the first minute. However, the performance declines significantly over time, dropping to 2.0×10^{-7} g/L/min at the end. This degradation highlights the unsustainable cavitation conditions which could be likely caused by dispersed energy across multiple holes.

In addition to performance metrics, the power consumption of the four configurations is also compared to assess their energy efficiency. Fig. 11 shows the power density values, i.e., power consumption per unit volume for microscale HC reactors used in this study at different pressures and two macroscale plates at 0.35 MPa [79].

From Fig. 11 it can be clearly seen that the microscale configurations are significantly more energy-efficient than the macroscale plates. For instance, Reactor 1 achieves the highest I_3^- concentration and reaction rate while consuming just 0.51 W/L, compared to the 19.83 W/L and 12.81 W/L consumed by Plate 1 and Plate 2, respectively. Similarly, Reactor 2 consumes only 1.72 W/L which is approximately 11 times less than Plate 1 and 7 times less than Plate 2; however, it has a higher value compared to Reactor 1 (about 3 times more). The superior energy efficiency of microscale reactors is attributed to their higher surface-to-volume ratios, which enhance localized cavitation events and optimize heat and mass transfer rates. Reactor 1 stands out for its ability to generate highly localized pressure gradients, resulting in frequent and energetic cavitation events promoting hot spots and pressure conditions conducive to •OH production. Reactor 2, on the other hand, supports broader cavitation zones and flow uniformity, leading to prolonged stability. The macroscale plates, despite their significantly more power consumption, demonstrate a far inferior performance, due to the inability to sustain cavitation over time.

As a result, Reactor 1 and Reactor 2 consistently outperform the macroscale plate designs in both I_3^- production and reaction rate while maintaining significantly lower power consumption. The trends observed in the Figs. 10 and 11 highlight the inherent advantages of "HC on a chip" reactors, and their ability to sustain cavitation intensity, to generate localized and intense pressure gradients, and to efficiently utilize energy. These advantages provide a solid proof for their suitability for applications requiring radical production, efficient chemical reactions, and energy savings. Table 3 presents a comparison between microscale and macroscale reactors in terms of maximum I_3^- concentration, production rate, and power density at the pressures where the maximum chemical effects of cavitation were observed. •OH generation during cavitation is governed by reactor geometry, flow dynamics, and reaction rate trends. Micro-orifice reactors exhibit sharp, high peaks of reaction rate due to intense, localized cavitation, while long diaphragm reactors display more gradual, sustained rates reflecting broader radical distribution. These differences significantly influence •OH yield, even under identical upstream conditions [39].

4. Conclusion

This study examines the relationship between cavitating flow dynamics and reactive species production in two microscale HC reactors. Reactor 1 configuration demonstrates a superior performance in generating high concentrations and I_3^- production, driven by its ability to induce intense localized pressure gradients, which promote frequent and powerful bubble collapses. This makes it highly effective for applications requiring rapid, concentrated chemical reactions, such as advanced oxidation processes in wastewater treatment. On the other hand, Reactor 2 exhibits lower cavitation yields; however, it offers a more uniform distribution of reactive species over prolonged reaction periods, making it ideal for processes demanding stable conditions, such as graphene production. The long diaphragm reactor exhibited a steady and gradual rate of I_3^- formation, indicating a more even distribution of radical generation along the length of the reactor. While the sharp peak seen in the micro-orifice design, suggesting less concentrated cavitation activity. The trend is supported by the geometry of the reactor, which accommodates long cavitation zones and long-duration bubble collapse processes. As the pressure increases, the transition to stable vapor cavities impacts radical production efficiency, emphasizing the critical balance between cavitation intensity and radical recombination. The core significance of cavitating flow patterns and topology of the geometry in enhancing the yield of hydroxyl radicals is highlighted. The findings of this study demonstrate the universality of microscale HC reactor, showing their ability to outperform the macroscale variants, which places them as top candidates to be employed. By modifying reactor designs to fit process-specific needs—whether fast radical formation is optimized or continuous chemical activity—this research

Table 3
Comparing chemical effects of HC collapse for microscale and macroscale.

Reactor	Maximum I_3^- production	Maximum reaction rate	Power density
Reactor 1 (at 0.52 MPa)	3.2×10^{-5} g/L	2.4×10^{-6} g/L/min at 12th min	0.51 W/L
Reactor 2 (at 2.07 MPa)	2.1×10^{-5} g/L	1.4×10^{-6} g/L/min at 10th min	1.72 W/L
Plate 1 [79] (at 0.35 MPa)	0.8×10^{-5} g/L	0.5×10^{-6} g/L/min at 4th min	19.83 W/L
Plate 2 [79] (at 0.35 MPa)	1.85×10^{-5} g/L	1.7×10^{-6} g/L/min at 1st min	12.81 W/L

forms the foundation for optimizing HC systems across a broad array of industrial purposes, enhancing chemical processing abilities with precision and efficacy.

Supplementary data to this article can be found online at https://doi.org/10.1016/j.cej.2025.164356.

CRediT authorship contribution statement

Rana Golshaei: Writing – original draft, Visualization, Validation, Methodology, Investigation, Formal analysis. **Salar Heyat Davoudian:** Writing – original draft, Visualization, Validation, Methodology, Investigation, Formal analysis. **Erçil Toyran:** Visualization, Investigation. **Ezgi Kestek:** Visualization. **Amanpreet Kaur:** Writing – review & editing, Methodology, Conceptualization. **Abhinav Priyadarshi:** Writing – review & editing, Investigation, Conceptualization. **Ali Koşar:** Writing – review & editing, Resources, Project administration, Methodology, Conceptualization. **Iakovos Tzanakis:** Writing – review & editing, Supervision, Resources, Project administration, Methodology, Funding acquisition, Conceptualization. **Morteza Ghorbani:** Writing – review & editing, Writing – original draft, Validation, Supervision, Resources, Project administration, Methodology, Investigation, Funding acquisition, Conceptualization.

Declaration of competing interest

The authors declare that they have no known competing financial interests or personal relationships that could have appeared to influence the work reported in this paper.

Acknowledgments

Data availability

Data will be made available on request.

References

[1] X. Sun, J.Y. Yoon, Multi-objective optimization of a gas cyclone separator using genetic algorithm and computational fluid dynamics, Powder Technol. 325 (2018) 347–360.
[2] K.S. Suslick, Sonochemistry, Science (1979) 247 (1990) 1439–1445.

[3] I. Tzanakis, D.G. Eskin, A. Georgoulas, D.K. Fytanidis, Incubation pit analysis and calculation of the hydrodynamic impact pressure from the implosion of an acoustic cavitation bubble, Ultrason. Sonochem. 21 (2014) 866–878.

[4] X. Sun, J. Liu, L. Ji, G. Wang, S. Zhao, J.Y. Yoon, et al., A review on hydrodynamic cavitation disinfection: the current state of knowledge, Sci. Total Environ. 737 (2020) 139606.

[5] M.T. Gevari, T. Abbasiasl, S. Niazi, M. Ghorbani, A. Koşar, Direct and indirect thermal applications of hydrodynamic and acoustic cavitation: a review, Appl. Therm. Eng. 171 (2020) 115065.

[6] M.B. Mane, V.M. Bhandari, K. Balapure, V.V. Ranade, Destroying antimicrobial resistant bacteria (AMR) and difficult, opportunistic pathogen using cavitation and natural oils/plant extract, Ultrason. Sonochem. 69 (2020) 105272.

[7] S. Weon, F. He, W. Choi, Status and challenges in photocatalytic nanotechnology for cleaning air polluted with volatile organic compounds: visible light utilization and catalyst deactivation, Environ. Sci. Nano 6 (2019) 3185–3214.

[8] M. Nabi, G. Zhang, P. Zhang, X. Tao, S. Wang, J. Ye, et al., Contribution of solid and liquid fractions of sewage sludge pretreated by high pressure homogenization to biogas production, Bioresour. Technol. 286 (2019) 121378.

[9] R.T. Hilares, J. Resende, C.A. Orsi, M.A. Ahmed, T.M. Lacerda, S.S. Da Silva, et al., Exopolysaccharide (pullulan) production from sugarcane bagasse hydrolysate aiming to favor the development of biorefineries, Int. J. Biol. Macromol. 127 (2019) 169–177.

[10] S. Rajoria, S. Rani, D. Chaudhari, S. Jain, U. Gupta, Glycine-poly-L-lactic acid copolymeric nanoparticles for the efficient delivery of bortezomib, Pharm. Res. 36 (2019) 1–15.

[11] F. Wu, X. Shi, H. Zou, T. Zhang, X. Dong, R. Zhu, et al., Effects of high-pressure homogenization on physicochemical, rheological and emulsifying properties of myofibrillar protein, J. Food Eng. 263 (2019) 272–279.

[12] Z. Zhang, H. Jin, C. Wu, J. Ji, Efficient production of high-quality few-layer graphene using a simple hydrodynamic-assisted exfoliation method, Nanoscale Res. Lett. 13 (2018) 1–8.

[13] G.E. Reisman, Y.-C. Wang, C.E. Brennen, Observations of shock waves in cloud cavitation, J. Fluid Mech. 355 (1998) 255–283.

[14] O. Supponen, D. Obreschkow, P. Kobel, M. Tinguely, N. Dorsaz, M. Farhat, Shock waves from nonspherical cavitation bubbles, Phys. Rev. Fluids 2 (2017) 093601.

[15] J. Luo, Z. Niu, Jet and shock wave from collapse of two cavitation bubbles, Sci. Rep. 9 (2019) 1352.

[16] A.A. Aganin, I.N. Mustafin, Outgoing shock waves at collapse of a cavitation bubble in water, Int. J. Multiphase Flow 144 (2021) 103792.

[17] J.-B. Li, W.-L. Xu, Y. Xia, M. Ye, Y.-W. Zhai, J. Deng, Effect of an air bubble on the collapse shock wave of a cavitation bubble, Ocean Eng. 297 (2024) 117094.

[18] M. Khavari, A. Priyadarshi, A. Hurrell, K. Pericleous, D. Eskin, I. Tzanakis, Characterization of shock waves in power ultrasound, J. Fluid Mech. 915 (2021) R3.

[19] M. Khavari, A. Priyadarshi, J. Morton, K. Porfyrakis, K. Pericleous, D. Eskin, et al., Cavitation-induced shock wave behaviour in different liquids, Ultrason. Sonochem. 94 (2023) 106328.

[20] F. Rokhsar Talabazar, A. Sheibani Aghdam, M. Jafarpour, D. Grishenkov, A. Koşar, M. Ghorbani, Chemical effects in "hydrodynamic cavitation on a chip": the role of cavitating flow patterns, Chem. Eng. J. 445 (2022) 136734, https://doi.org/10.1016/J.CEJ.2022.136734.

[21] Y.L. Pang, A.Z. Abdullah, S. Bhatia, Review on sonochemical methods in the presence of catalysts and chemical additives for treatment of organic pollutants in wastewater, Desalination 277 (2011) 1–14.

[22] X. Sun, J. Liu, L. Ji, G. Wang, S. Zhao, J.Y. Yoon, et al., A review on hydrodynamic cavitation disinfection: the current state of knowledge, Sci. Total Environ. 737 (2020) 139606.

[23] M. Gagol, E. Cako, K. Fedorov, R.D.C. Soltani, A. Przyjazny, G. Boczkaj, Hydrodynamic cavitation based advanced oxidation processes: studies on specific effects of inorganic acids on the degradation effectiveness of organic pollutants, J. Mol. Liq. 307 (2020) 113002.

[24] A.V. Mohod, A.C.S.C. Teixeira, M.V. Bagal, P.R. Gogate, R. Giudici, Degradation of organic pollutants from wastewater using hydrodynamic cavitation: a review, J. Environ. Chem. Eng. 11 (2023) 109773.

[25] T.N. Viten`ko, Y.M. Gumnitskii, A mechanism of the activating effect of hydrodynamic cavitation on water, J. Water Chem. Technol. 29 (2007) 231–237.

[26] Q. Xiang, J. Yu, P.K. Wong, Quantitative characterization of hydroxyl radicals produced by various photocatalysts, J. Colloid Interface Sci. 357 (2011) 163–167.

[27] S. Pei, S. You, J. Ma, X. Chen, N. Ren, Electron spin resonance evidence for electro-generated hydroxyl radicals, Environ. Sci. Technol. 54 (2020) 13333–13343.

[28] A. Martinez-Tarifa, S. Arrojo, O. Louisnard, J. González-García, I. Tudela, Correlation between hydroxyl radical production and theoretical pressure distribution in a sonochemical reactor, Phys. Procedia 3 (2010) 971–979.

[29] O. Moussous, S. Khoudri, M. Benguerba, Characterization of a Fricke dosimeter at high energy photon and electron beams used in radiotherapy, Australas. Phys. Eng. Sci. Med. 34 (2011) 523–528.

[30] A. Ebrahiminia, M. Mokhtari-Dizaji, T. Toliyat, Correlation between iodide dosimetry and terephthalic acid dosimetry to evaluate the reactive radical production due to the acoustic cavitation activity, Ultrason. Sonochem. 20 (2013) 366–372.

[31] J. Rooze, E.V. Rebrov, J.C. Schouten, J.T.F. Keurentjes, Dissolved gas and ultrasonic cavitation – a review, Ultrason. Sonochem. 20 (2013) 1–11, https://doi.org/10.1016/J.ULTSONCH.2012.04.013.

[32] K.R. Morison, C.A. Hutchinson, Limitations of the Weissler reaction as a model reaction for measuring the efficiency of hydrodynamic cavitation, Ultrason. Sonochem. 16 (2009) 176–183.

[33] A. Ebrahiminia, M. Mokhtari-Dizaji, T. Toliyat, Correlation between iodide dosimetry and terephthalic acid dosimetry to evaluate the reactive radical production due to the acoustic cavitation activity, Ultrason. Sonochem. 20 (2013) 366–372.

[34] M. Paquin, É. Loranger, V. Hannaux, B. Chabot, C. Daneault, The use of Weissler method for scale-up a Kraft pulp oxidation by TEMPO-mediated system from a batch mode to a continuous flow-through sonoreactor, Ultrason. Sonochem. 20 (2013) 103–108.

[35] R. Pflieger, S.I. Nikitenko, M. Ashokkumar, Effect of NaCl salt on sonochemistry and sonoluminescence in aqueous solutions, Ultrason. Sonochem. 59 (2019) 104753.

[36] S. Gligorovski, R. Strekowski, S. Barbati, D. Vione, Environmental implications of hydroxyl radicals (•OH), Chem. Rev. 115 (2015) 13051–13092, https://doi.org/10.1021/cr500310b.

[37] S. Altenhöfer, K.A. Radermacher, P.W.M. Kleikers, K. Wingler, H.H.H.W. Schmidt, Evolution of NADPH oxidase inhibitors: selectivity and mechanisms for target engagement, Antioxid. Redox Signal. 23 (2015) 406–427.

[38] B. Halliwell, J.M.C. Gutteridge, Free radicals in Biology and Medicine, Oxford University Press, 2015.

[39] K.-S. Im, S.-K. Cheong, C.F. Powell, M.D. Lai, J. Wang, Unraveling the geometry dependence of in-nozzle cavitation in high-pressure injectors, Sci. Rep. 3 (2013) 2067.

[40] A. Simpson, V.V. Ranade, Modelling of hydrodynamic cavitation with orifice: influence of different orifice designs, Chem. Eng. Res. Des. 136 (2018) 698–711, https://doi.org/10.1016/j.cherd.2018.06.014.

[41] X. Long, J. Zhang, J. Wang, M. Xu, Q. Lyu, B. Ji, Experimental investigation of the global cavitation dynamic behavior in a venturi tube with special emphasis on the cavity length variation, Int. J. Multiphase Flow 89 (2017) 290–298, https://doi.org/10.1016/j.ijmultiphaseflow.2016.11.004.

[42] M. Medrano, P.J. Zermatten, C. Pellone, J.P. Franc, F. Ayela, Hydrodynamic cavitation in microsystems. I. Experiments with deionized water and nanofluids, Phys. Fluids 23 (2011) 127103, https://doi.org/10.1063/1.3671682.

[43] K. Kerboua, O. Hamdaoui, A. Alghyamah, Energy balance of high-energy stable acoustic cavitation within dual-frequency sonochemical reactor, Ultrason. Sonochem. 73 (2021) 105471, https://doi.org/10.1016/j.ultsonch.2021.105471.

[44] F. Hong, H. Xue, X. Yuan, L. Wang, H. Tian, L. Ye, et al., Numerical investigation on the hydrodynamic performance with special emphasis on the cavitation intensity detection in a Venturi cavitator, Process Saf. Environ. Prot. 175 (2023) 212–226, https://doi.org/10.1016/j.psep.2023.05.037.

[45] A.S. Lobasov, Ayu Kravtsova, The effect of a textured surface in the form of triangular prisms on the occurrence and development of cavitation behind the cylinder in microchannels, Phys. Fluids 36 (2024) 073309, https://doi.org/10.1063/5.0214411.

[46] M. Maleki, F. Rokhsar Talabazar, S. Heyat Davoudian, M. Dular, A. Koşar, M. Petkovšek, et al., The formation of hydroxyl radicals during hydrodynamic cavitation in microfluidic reactors using salicylic acid dosimetry, Chem. Eng. J. 511 (2025) 161976, https://doi.org/10.1016/j.cej.2025.161976.

[47] M.T. Angaji, R. Ghiaee, Decontamination of unsymmetrical dimethylhydrazine waste water by hydrodynamic cavitation-induced advanced Fenton process, Ultrason. Sonochem. 23 (2015) 257–265.

[48] W. Ding, F. Hong, D. Ying, Y. Huang, S.N. Khan, J. Jia, A comprehensive study on the effects of annular protrusion for cavitation intensification in Venturi tubes, Chem. Eng. J. 498 (2024) 155306.

[49] X.-Y. Duan, B.-H. Huang, Y.-X. Zhu, X. Song, C.-Y. Zhu, J.C. Chai, et al., Cavitating flows in microchannel with rough wall using a modified microscale cavitation model, Case Stud. Therm. Eng. 52 (2023) 103735.

[50] M. Ghorbani, A.K. Sadaghiani, L.G. Villanueva, A. Koşar, Hydrodynamic cavitation in microfluidic devices with roughened surfaces, J. Micromech. Microeng. 28 (2018) 075016, https://doi.org/10.1088/1361-6439/aab9d0.

[51] B. Kratochvíl, V. Mornstein, Use of chemical dosimetry for comparison of ultrasound and ionizing radiation effects on cavitation, Physiol. Res. 56 (2007) S77.

[52] K. Agarwal, O. Ram, Y. Lu, J. Katz, On the pressure field, nuclei dynamics and their relation to cavitation inception in a turbulent shear layer, J. Fluid Mech. 966 (2023) A31.

[53] E.P. Rood, Mechanisms of Cavitation Inception, 1991.

[54] M. Adama Maiga, O. Coutier-Delgosha, D. Buisine, A new cavitation model based on bubble-bubble interactions, Phys. Fluids 30 (2018) 123301, https://doi.org/10.1063/1.5052257.

[55] J. Choi, C.-T. Hsiao, G. Chahine, S. Ceccio, Growth, oscillation and collapse of vortex cavitation bubbles, J. Fluid Mech. 624 (2009) 255–279.

[56] M. Medrano, C. Pellone, P.J. Zermatten, F. Ayela, Hydrodynamic cavitation in microsystems. Part II. Simulations and optical observations, Phys. Fluids 24 (2012).

[57] M. Bhatt, K. Mahesh, Numerical investigation of partial cavitation regimes over a wedge using large eddy simulation, Int. J. Multiphase Flow 122 (2020) 103155.

[58] D. Podbevšek, M. Petkovšek, C.D. Ohl, M. Dular, Kelvin-Helmholtz instability governs the cavitation cloud shedding in Venturi microchannel, Int. J. Multiphase Flow 142 (2021) 103700.

[59] M. Maleki, F. Rokhsar Talabazar, A. Koşar, M. Ghorbani, On the spatio-temporal dynamics of cavitating turbulent shear flow over a microscale backward-facing step: a numerical study, Int. J. Multiphase Flow 177 (2024) 104875, https://doi.org/10.1016/j.ijmultiphaseflow.2024.104875.

[60] S. Arrojo, C. Nerín, Y. Benito, Application of salicylic acid dosimetry to evaluate hydrodynamic cavitation as an advanced oxidation process, Ultrason. Sonochem. 14 (2007) 343–349.

[61] M. Capocelli, D. Musmarra, M. Prisciandaro, A. Lancia, Chemical effect of hydrodynamic cavitation: simulation and experimental comparison, AIChE J 60 (2014) 2566–2572.

[62] S.J. De-Nasri, V.P. Sarvothaman, S. Nagarajan, P. Manesiotis, P.K.J. Robertson, V. V. Ranade, Quantifying OH radical generation in hydrodynamic cavitation via coumarin dosimetry: influence of operating parameters and cavitation devices, Ultrason. Sonochem. 90 (2022) 106207, https://doi.org/10.1016/J. ULTSONCH.2022.106207.

[63] P.R. Gogate, A.B. Pandit, Hydrodynamic cavitation reactors: a state of the art review, Rev. Chem. Eng. 17 (2001) 1–85.

[64] M. Ghorbani, The hydrodynamic cavitation manifestation in small chips, IEEE Access 9 (2021) 110517–110524.

[65] J. Rooze, M. André, G.-J.S. van der Gulik, D. Fernández-Rivas, J.G.E. Gardeniers, E. V. Rebrov, et al., Hydrodynamic cavitation in micro channels with channel sizes of 100 and 750 micrometers, Microfluid. Nanofluid. 12 (2012) 499–508, https://doi. org/10.1007/s10404-011-0891-5.

[66] X. Fang, M.F. Tachie, Spatio-temporal dynamics of flow separation induced by a forward-facing step submerged in a thick turbulent boundary layer, J. Fluid Mech. 892 (2020) A40.

[67] S. Nishimura, O. Takakuwa, H. Soyama, Similarity law on shedding frequency of cavitation cloud induced by a cavitating jet, J. Fluid Sci. Technol. 7 (2012) 405–420.

[68] M. Ylönen, J.-P. Franc, J. Miettinen, P. Saarenrinne, M. Fivel, Shedding frequency in cavitation erosion evolution tracking, Int. J. Multiphase Flow 118 (2019) 141–149.

[69] C. Peng, S. Tian, G. Li, Determination of the shedding frequency of cavitation cloud in a submerged cavitation jet based on high-speed photography images, J. Hydrodyn. 33 (2021) 127–139.

[70] M. Maleki, F. Rokhsar Talabazar, E. Toyran, A. Priyadarshi, A. Sheibani Aghdam, L. G. Villanueva, et al., New insights on cavitating flows over a microscale backward-facing step, Phys. Fluids 36 (2024) 093335, https://doi.org/10.1063/5.0225030.

[71] A. Šarc, T. Stepišnik-Perdih, M. Petkovšek, M. Dular, The issue of cavitation number value in studies of water treatment by hydrodynamic cavitation, Ultrason. Sonochem. 34 (2017) 51–59, https://doi.org/10.1016/J.ULTSONCH.2016.05.020.

[72] K. Yasui, Production of O radicals from cavitation bubbles under ultrasound, Molecules 27 (2022) 4788.

[73] C. Mishra, Y. Peles, Cavitation in flow through a micro-orifice inside a silicon microchannel, Phys. Fluids 17 (2004) 013601, https://doi.org/10.1063/ 1.1827602.

[74] C. Mishra, Y. Peles, An experimental investigation of hydrodynamic cavitation in micro-Venturis, Phys. Fluids 18 (2006) 103603, https://doi.org/10.1063/ 1.2360996.

[75] Y.-C. Wang, C.E. Brennen, The noise generated by the collapse of a cloud of cavitation bubbles, ASME-PUBLICATIONS-FED 226 (1995) 17–30.

[76] T. Wang, C. Yang, P. Sun, M. Wang, F. Lin, M. Fiallos, et al., Generation mechanism of hydroxyl free radicals in micro–nanobubbles water and its prospect in drinking water, Processes 12 (2024) 683.

[77] M. Dular, T. Griessler-Bulc, I. Gutierrez-Aguirre, E. Heath, T. Kosjek, A. Krivograd Klemenčič, et al., Use of hydrodynamic cavitation in (waste)water treatment, Ultrason. Sonochem. 29 (2016) 577–588, https://doi.org/10.1016/J. ULTSONCH.2015.10.010.

[78] https://www.globalpetrolprices.com/Turkey/electricity_prices/ n.d.

[79] P. Senthil Kumar, M. Siva Kumar, A.B. Pandit, Experimental quantification of chemical effects of hydrodynamic cavitation, Chem. Eng. Sci. 55 (2000) 1633–1639, https://doi.org/10.1016/S0009-2509(99)00435-2.

[80] K. Yasui, Y. Iida, T. Tuziuti, T. Kozuka, A. Towata, Strongly interacting bubbles under an ultrasonic horn, Phys. Rev. E 77 (2008) 016609.

[81] L. Stricker, B. Dollet, D. Fernández Rivas, D. Lohse, Interacting bubble clouds and their sonochemical production, J. Acoust. Soc. Am. 134 (2013) 1854–1862.